Electronic Supplementary Material (ESI) for Lab on a Chip.
This journal is © The Royal Society of Chemistry 2016

ELECTRONIC SUPPLEMENTARY INFORMATION

Through thick and thin: a microfluidic approach for continuous measurements of biofilm viscosity and the effect of ionic strength

F. Paquet-Mercier,[a] M. Parvinzadeh Gashti,[a] J. Bellavance,[a] S.M. Taghavi,[b] J. Greener[a,*]

1. *Parallel microfluidic biofilm flow culture device:*

Each microfluidic device contained six flow cells, each containing an inlet, outlet and a glass microscope coverslip. A schematic of one flow cell is shown in Figure S1a. Method of fabrication, dimensions and other relevant information are given in the main paper. Figure S1b shows the microfluidic device interfaced with a microscope and computer-controlled stage for accurate placement of the field of view. The system did not have auto-focus, so care had to be taken during mounting the device on the microscope stage to ensure that all channels were in the same focal plane.

(a) (b)

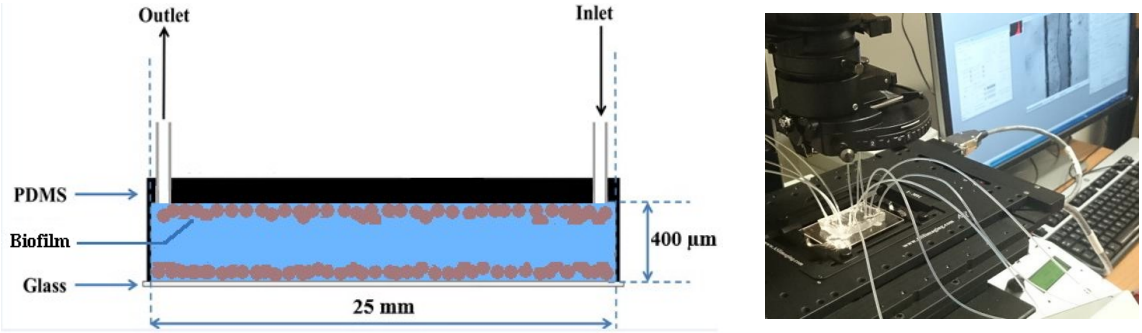

Figure S1. (a) Schematic of a single microfluidic flow cell. (b) A six-channel microfluidic flow cell connected to syringe pump, is mounted on an automatic microscope stage.

2. *Velocity measurements in different locations of the microchannel:*

Figure S2 shows a typical average net velocity, $\tilde{v}_{net}$, versus time for moving biofilm segments for a separate experiment, which was conducted with bacteria from different pre-culture than experiments shown in the main paper. At 8 h, visible biofilm segments began to form in the channel. Shortly after, they began to flow downstream under the shear force of the flowing nutrient solution. In this experiment the $\tilde{v}_{net}$ steadily grew until it reached its maximum value of 64.3 $\mu m \cdot h^{-1}$ at t=34 h. A shoulder was also noted in the $\tilde{v}_{net}$ versus time curve. A fitting algorithm using a 2 Gaussian composite peak, found a broad peak centred at t=31 h and a second taller and sharper peak centred at t=34 h. This was attributed to a bimodal distribution of $\tilde{v}_{net}$ values, one far from and one close to the vertical side-walls, due to strongly varying shear stresses. Numerical simulations were conducted using COMSOL multiphysics (v4.2) using physics for "Laminar Flow" and "Transport of Dilute Species" and free tetrahedral meshing with "fine" resolution revealed that the variations to the shear stress at the vertical side-walls became insignificant at a distance of more than 100 µm from the wall (Figure S2 inset). Based on these results, we obtained measurements of $\tilde{v}_{net}$ from the centre portion of the channel to avoid differences between experimental and calculated shear stress.

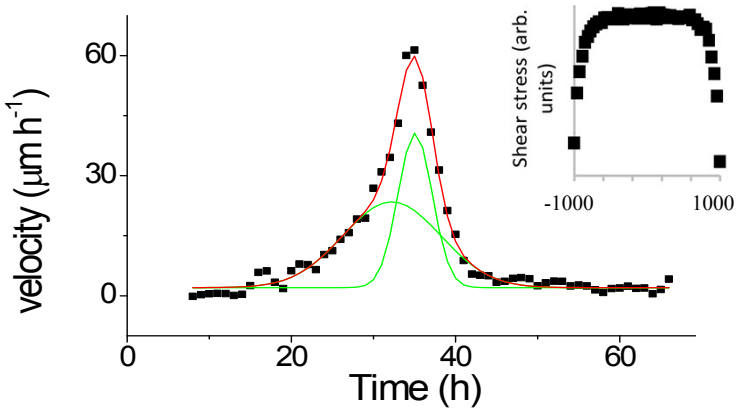

Figure S2. Time-dependent $\tilde{v}_{net}$ of tracked biofilm segments (black squares) obtained from a biofilm growing under nutrient solution containing 0.1 wt% NaCl. The red curve is the fitting

results using a 2 Gaussian peak model, with the de-convoluted peaks in green. Each point represents the average from 40 different tracked biofilm segments. The inset profiles the change in applied shear stress for different positions along the channel cross-section.

3. Error bands via 95% confidence interval:

In this work we showed either the 95% confidence interval or the standard deviation (STD) with of sample size (n) reported for measurements velocity, height and viscosity. Sample size was typically close to n=50, which approximately equates to a confidence interval of 0.84xSTD to 1.25xSTD. To simplify the plots, we used "error bands" instead of error bars, which project a solid colour background marking the area around the mean values which are statistically significant. The exact mean values are represented by data points. Error bands were created by expanding the line width of the error bars so that they touched each other followed by smoothing, giving the appearance of a continuous background over which data points were placed. In some cases, where the standard deviations were small (e.g. Fig. 4 in the main paper) the band seems discontinuous. In the case of Figures 5 and 7 in the main paper, where there were multiple $\tilde{v}_{net}$ and $\mu_{biofilm}$ trends in the same figure, no error bands were presented to avoid crowding in the plot. These cases are dealt with in the next two sections.

4. Upper and lower limits in 95% confidence intervals for $\tilde{v}_{net}$:

Statistical analysis of biofilm segments $\tilde{v}_{net}$ grown under different ionic strengths were excluded from Figure 5a (main paper) for clarity. Here we show the 95% confidence interval (CI) in the standard deviation (STD) of $\tilde{v}_{net}$ for each experiment separately. The CI limits for each time were normalized by $\tilde{v}_{net}$ as shown in Eqs (S1) and (S2). In other words we calculated the coefficient of variance (CV) for the upper and lower CI values.

$$CV_{CIupper} = CI_{upper}/\tilde{v}_{net} \quad \text{(S1)}$$

$$CV_{CIlower} = CI_{lower}/\tilde{v}_{net} \quad \text{(S2)}$$

Figure S3 shows the CV of 95% CI limits for the different NaCl concentration conditions used in this paper and reports n for each case.

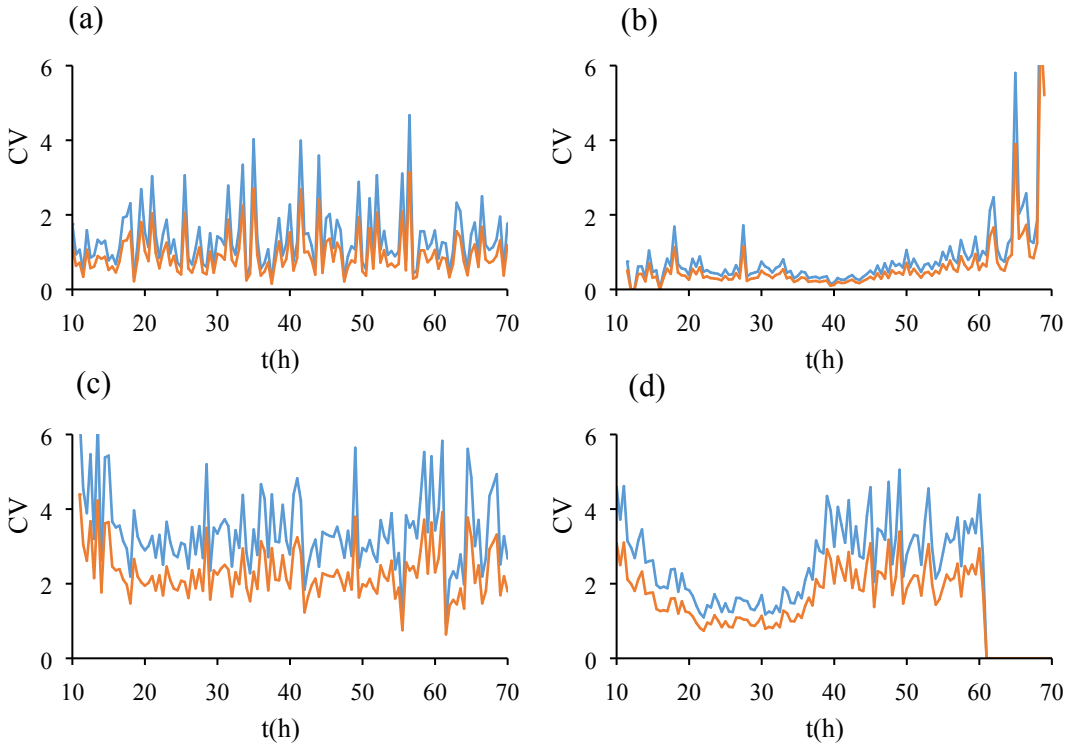

Figure S3. Coefficient of variance of upper (blue) and lower (orange) confidence intervals (95%) in the standard deviation of $\tilde{v}_{net}$. Number of tracks, n, and [NaCl] were (a) 46, 0 wt%, (b) 48, 0.05 wt%, (c) 51, 0.1 wt%, and (d) 55, 0.2 wt%.

5. Upper and lower limits for 95% confidence intervals for $\mu_{biofilm}$:

Statistical analysis of biofilm segments' $\mu_{biofilm}$ grown under different ionic strengths were excluded from Figure 7a (main paper) for clarity. Here we show the 95% confidence interval (CI) in the standard deviation (STD) of $\mu_{biofilm}$ for each experiment separately. The CI limits for each time are normalized by $\mu_{biofilm}$ as shown in Eqs. (S1) and (S2). In other words we calculate the coefficient of variance (CV) for the upper and lower CI values.

$$CV_{CIupper} = CI_{upper}/\mu_{biofilm} \quad \text{(S3)}$$

$$CV_{CIlower} = CI_{lower}/\mu_{biofilm} \quad \text{(S4)}$$

Figure S4 shows the CV of 95% CI limits for the different NaCl concentration conditions used in this paper and reports n for each case. We note that in the case of 0 wt% and 0.1 wt%, the CI is quite low compared to $\mu_{biofilm}$. For 0.2%, the normalized values of CI are relatively high.

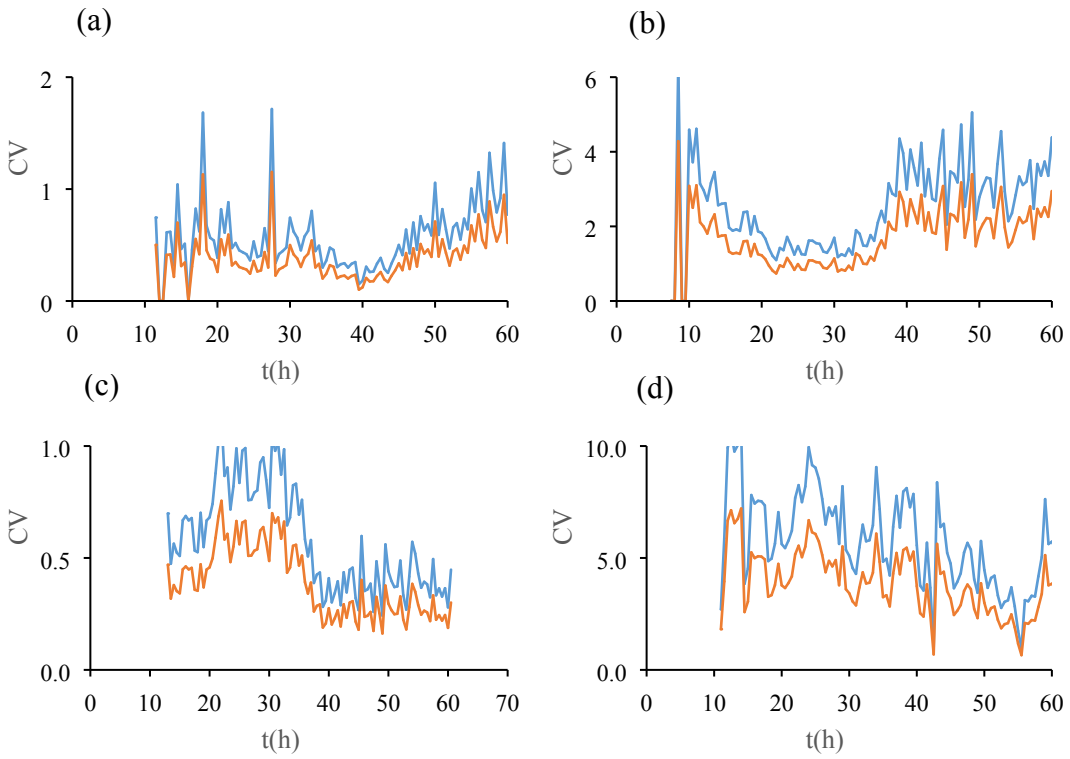

Figure S4. Coefficient of variance of upper (blue) and lower (orange) confidence intervals (95%) in the standard deviation of $\mu_{biofilm}$. Number of tracks, n, and [NaCl] were (a) 46, 0 wt%, (b) 48, 0.05 wt%, (c) 51, 0.1 wt%, and (d) 55, 0.2 wt%.

6. Growth kinetics:

Figure S5 shows the measured optical density (OD) as a function of time for biofilms grown under three different NaCl concentrations. These are from the same experiments discussed in the main paper. The semi-log plot shows that the exponential growth region for each biofilm occurs before 20 h. In all cases, the mature phase, where the OD does not increase further, is after 40 h.

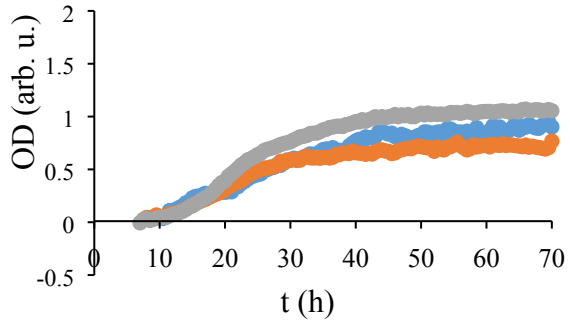

Figure S5. Semi-log plot of time-dependent changes to OD and for biofilms grown under modified LB nutrient solutions with NaCl concentrations 0.05 wt% (blue), 0.1 wt% (orange), 0.2 wt% (grey).

7. Structural heterogeneity:

Structural heterogeneity was measured via coefficient of variance (CV) of the entire channel as a preferred method over pixel intensity standard deviation (I_{STD}).[1] CV was calculated for each time step as $CV = I_{STD}/I_{AVE}$, where I_{AVE} is the average pixel intensity (Fig. S6). We note that structural heterogeneity decreased with increasing ionic strength of the nutrient solution.

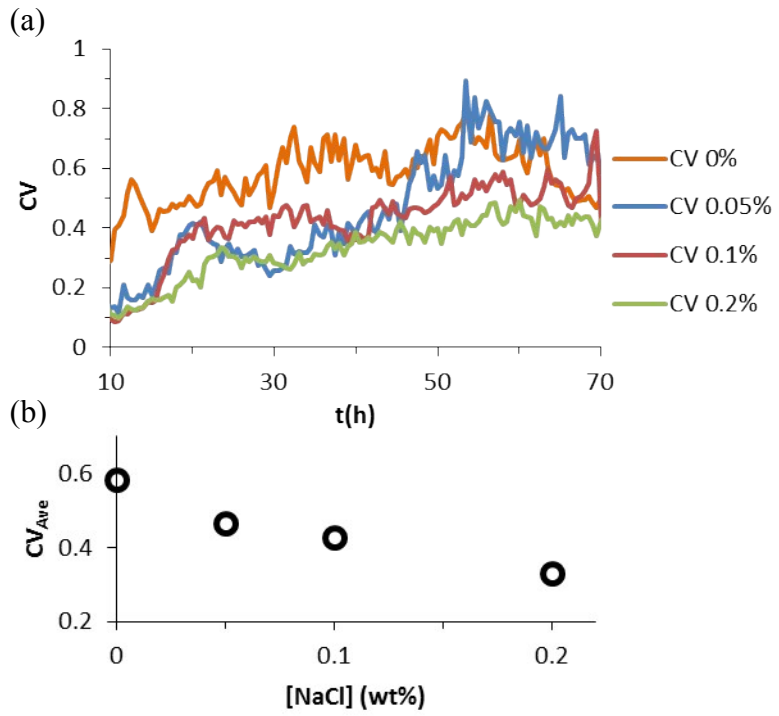

Figure S6. (a) CV for biofilms grown under LB nutrient solutions containing [NaCl] of 0 wt% (orange), 0.05 wt% (blue), 0.1 wt% (red), 0.2wt% (green). (b) Average CV (CV_{Ave}) from biofilms in (a) in the time interval 10-70 hours versus [NaCl].

8. Calibrated height measurements using optical density:

Figure 6 in the main paper showed separate *h* versus time plots. Figure S7 shows the three data sets acquired with [NaCl] > 0 in the same plot without error bands for easier viewing. Their trends are very similar with h for [NaCl] = 0.05 wt% lagging a little behind the others for 20 h following the exponential growth phase. There are no obvious correlations between *h* profiles and the onset of rapid thickening.

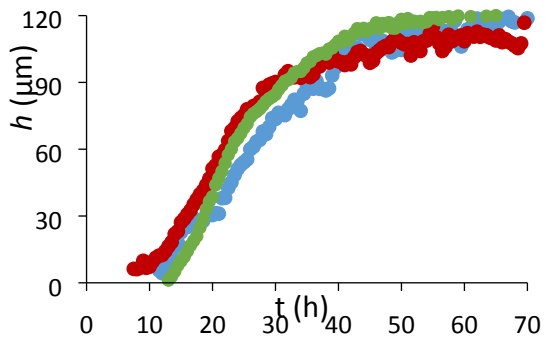

Figure S7. Plot of time-dependent *h* for biofilms grown under modified LB nutrient solutions with NaCl concentrations 0.05 wt% (blue), 0.1 wt% (red), 0.2 wt% (green).

9. CLSM measurements:

9a. Height measurements

In order to confirm *h* from OD, CLSM was used. The 3D confocal stacks were analyzed using the Fiji bundle for ImageJ. For each time frame, the intensity for each slice of the confocal stack was measured in the vicinity of moving biofilm structures. These measurements resulted in multiple curves similar to those in Figure S8. From these curves the biofilm height was measured by measuring their maximum width. As the early biofilm was composed of short segments, this measurement was harder to define than for thicker biofilms in later growth phases. In conjunction with limitations in z-resolution of CLSM measurements due to the 10x objective used, this is likely the reason that biofilm height is overestimated for the first time points in Figure 3 in the main paper.

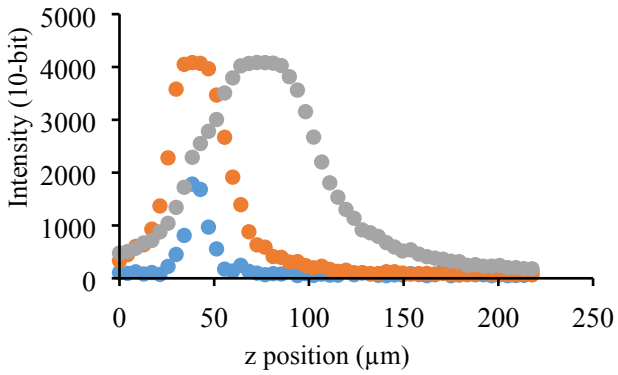

Figure S8. Intensity at different z position for some biofilm segments after 12, 24.5 and 39.5 h (blue, orange and grey, respectively). Biofilm *h* was measured by taking the width of the curves. Objective used was 10× which gave z-resolution of approximately 5 µm.

9b. Low-resolution measurements of upper and lower attachment surfaces

Confocal measurements of biofilms growing in the microchannel were obtained using a 4x objective due to its long working distance. This allowed imaging of both channel top and bottom at the same time, at the expense of a strongly reduced resolution (30 µm). Figure S9 shows the results from a 50 h old biofilm (after the average *h* became maximum) in a volume segment with width (perpendicular to channel), depth (parallel to channel) and height of 1600, 300 and 400 µm. The depth of 300 µm was chosen to simplify the two-dimensional representation of the three—dimensional data. The width of 1600 µm was the limit based on the objective used, which was centered in the channel middle where flow velocities were expected to be uniform and unaffected by side-walls. The slice was chosen because it contained the tallest features that could be found. The image shows patchy and non-interacting biofilm growth occurred on both sides of the channel but they do not interact with each other. Note that due to converging perspective lines, the low image resolution and the image processing, exact heights and widths of the biofilm segments cannot be read directly from the image.

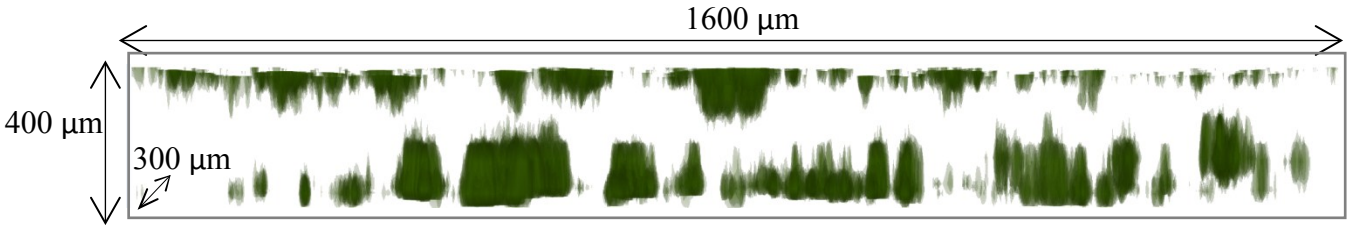

Figure S9. Rendering of a three-dimensional volume segment for a 50 h old *Pseudomonas sp.* biofilm (grown under modified LB nutrient solution containing NaCl concentration 0.1 wt%), with dimensions (width, depth, height) 1600, 300 and 400 μm. Imaging from CLSM with 4x objective and z-resolution of approximately 30 μm. A smoothing algorithm and a threshold limit of 50 were applied to remove noise and image "haze" from signal bleed from out of plane light.

9c. Medium-resolution measurements of a typical moving biofilm segment

A better image of a typical biofilm segment was obtained by CLSM with a 10× objective (Fig. S10). This reduced the working distance but improved the z-resolution to about 5 μm.

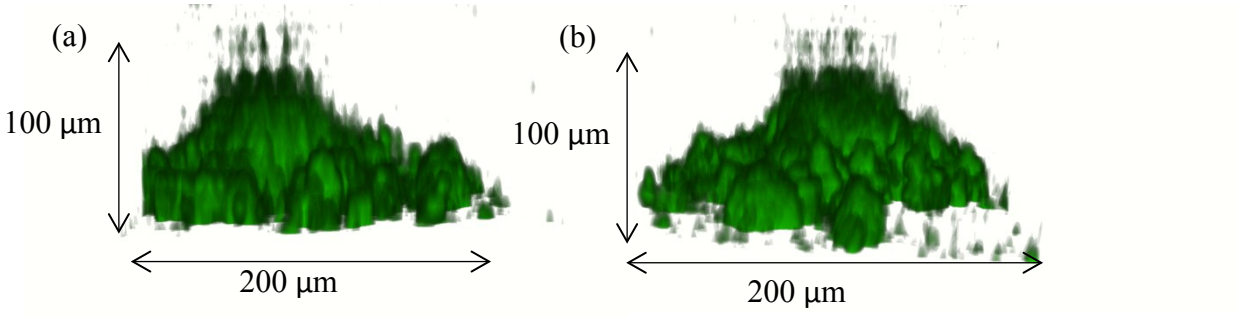

Figure S10. Rendering of a 38 h old *Pseudomonas sp.* biofilm segment (grown under modified LB nutrient solution containing NaCl concentration 0.1 wt%) near the middle of the channel against the glass sealing layer in the xz (a) and yz (b) planes. The 12-bit CLSM image stack was acquired with a 10× objective. Three-dimensional display volume has dimensions (width, depth, height) 200, 200 and 120 μm with z-resolution of approximately 5 μm. Image rendering was achieved using ImageJ "3D viewer". A smoothing algorithm and a threshold limit of 50 were applied to remove noise and image "haze" from signal bleed from out of plane light.

10. Passivity of CLSM measurements:

In order to verify that photoinduced stresses imposed during CLSM did not affect measurements we looked for evidence of photobleaching or changes to biofilm behaviour under different irradiation conditions. This was accomplished by double exposing the biofilm within a 40x objective (field of view 316.8 x 316.8 μm) during the acquisition time 23 min, which was centered within a larger 10x field of view during the acquisition time of 10 min. By comparing the intensities of the biofilms across all regions of the 10x field of view (including those which were double exposed in the 40 field of view), we noted that biofilm behaviour (growth and movement) and intensity were consistent in both the double- and single-exposed portions. Therefore, we concluded that CLSM measurements did not result in noticeable photobleaching of GFP or photodamage to bacteria.

11. ATR-FTIR:

ATR-FTIR Setup: ATR-FTIR spectra were acquired using a Nicolet Magna-850 infrared spectrometer (Thermo Scientific, Madison, WI) equipped with a Golden Gate single-bounce diamond ATR accessory (Specac Ltd., London, UK) measuring 2x2 mm. The microchannel was placed over the diamond crystal such that the crystal fit within the channel so that there would be no interfering signal from PSMS. The device was pressed against the ATR accessory with enough pressure to prevent leaking. A mercury cadmium telluride (MCT) narrow band detector cooled with liquid nitrogen was used. Spectral resolution was set a 4 cm^{-1}.

ATR-FTIR Results: Attenuated total reflection Fourier transform spectroscopy (ATR-FTIR) can follow vibrational bands associated with different chemical bonds, in time. We moniored the development of Amide II and PO_2 bands. The latter is related to bacterial nucleic acids, whereas

the former is seen in both EPS and bacteria. Two reductions in the growth of each molecule are interpreted as reduction in the molecular concentrations at the ATR sensing surface. This has previously been associated with so-call restructuring at the surface, whereby bacteria move away from the surface and pore structure begins to form. The second such event (marked with arrows in Fig. S11), appear to occur close in time to rapid thickening process noted in the paper.

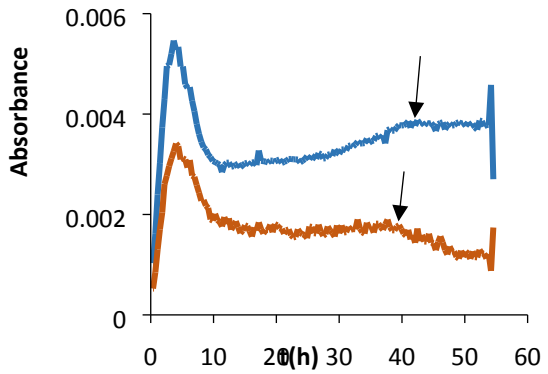

Figure S11. Spectra from a single experiment conducted under the same conditions as those in the main paper (and [NaCl]=0.1 wt%), with the exception that the microscope slide sealing wall was replaced by the ATR crystal. Absorbance for PO_2 (orange) and Amide II (blue).

12. Streamer formation:

We note the observation of streamer formation by a recently reported mechanism called "sudden partial detachment".[2] The reader is referred to that paper which provides thorough presentation of the phenomenon and images. Here we show an example of the same mode of streamer formation observed during these experiments. Figure S12 shows a portion of biofilm that moves from right to left in a counter clockwise type motion between 70 to 72 h. This is due to a partial detachment at the upstream side (right) while maintain a tether to the large, causing a rotational

motion. Background subtracted images show streamer more clearly with minimized interference from the heterogeneous background.

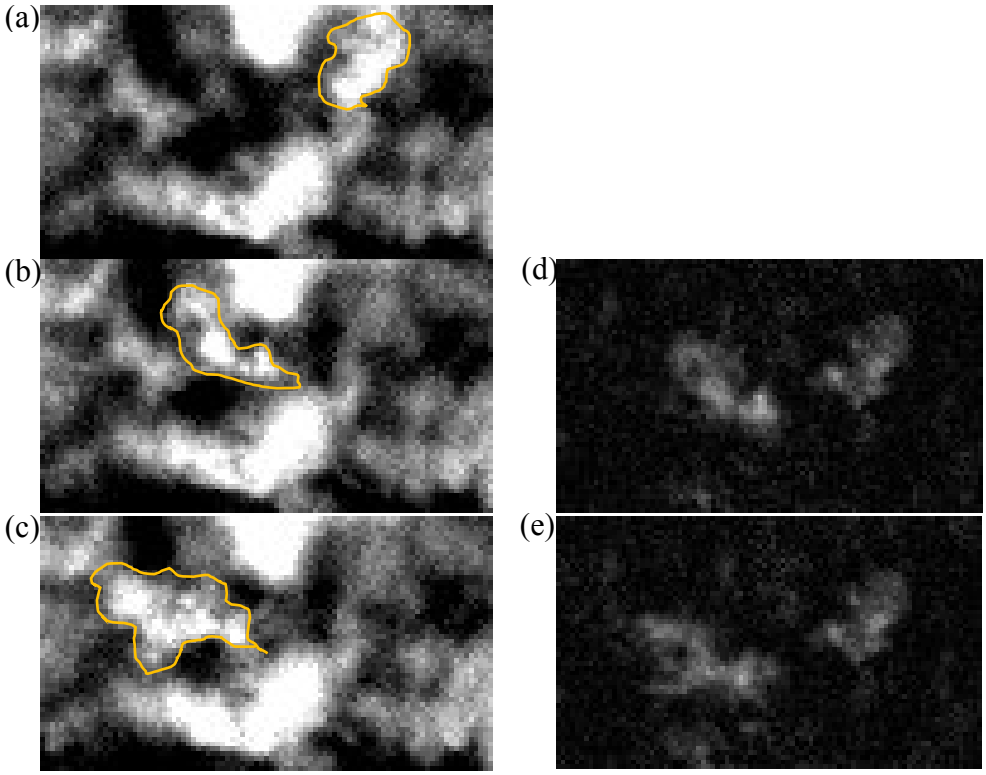

Figure S12. Partial detachment of a portion of a biofilm under flow from right to left. Images are acquired at (a) t=70 h,(b) t=71 h, (c) t=72 h after inoculation. Yellow boarder encircles the (pre-) streamer. The heterogeneous background was eliminated from the field of view by using the image from (a) as a background for the images in (b) and (c) to produce images in (d) and (e).

13. References:

Z. Lewandowski, H. Beyenal, Fundamentals of biofilm research, Taylor & Francis, New York, **2014**.

[2] M. Parvinzadeh Gashti, J. Bellavance, M. Kroukamp, G. Wolfaardt, S.M. Taghavi, J. Greener, "Live-streaming: Time-lapse video evidence of novel streamer formation mechanism and varying viscosity", *Biomicrofluidics*, **2015**, 9, 041101.